A novel biomimetic sensor system for vibration source perception of autonomous underwater vehicles based on artificial lateral lines

OPEN ACCESS
IOP Publishing
Measurement Science and Technology
Meas. Sci. Technol. **29** (2018) 125102 (17pp)
https://doi.org/10.1088/1361-6501/aae128

A novel biomimetic sensor system for vibration source perception of autonomous underwater vehicles based on artificial lateral lines

Guijie Liu[1,4], Shuxian Gao[1], Th Sarkodie-Gyan[2] and Zhixiong Li[3,4]

[1] Department of Mechanical and Electrical Engineering & Key Laboratory of Ocean Engineering of Shang Dong Province, Ocean University of China, Qingdao 266100, People's Republic of China
[2] College of Engineering, University of Texas, 500 W University Ave, El Paso, TX 79968, United States of America
[3] School of Mechanical, Materials, Mechatronic and Biomedical Engineering, University of Wollongong, Wollongong, NSW 2522, Australia

E-mail: liuguijie@ouc.edu.cn and zhixiong.li@ieee.org

Received 2 July 2018, revised 10 September 2018
Accepted for publication 13 September 2018
Published 23 October 2018

Abstract

The perception of vibration sources can be used to detect, classify, locate, and track autonomous underwater vehicles (AUVs), which is of great importance for ocean scientific research and naval applications. The artificial lateral lines system (ALLS) is a promising technique to sense underwater vibration sources. However, most current ALLS research focuses on perception mechanism and biomimetic sensor design. The design of a systematic ALLS that is ready for practical applications is still an unsolved problem. To this end, a novel biomimetic sensor system is proposed in this work for the purpose of developing a practical ALLS for AUVs. In order to determine the distribution of the developed biomimetic sensors in the AUVs, hydromechanics modelling and simulation of the artificial lateral lines were implemented to investigate the pressure response mechanisms of the AUVs in terms of the position, frequency and amplitude of the vibration source(s). Subsequently, an experimental AUV was equipped with biomimetic sensors to evaluate the performance of the vibration source perception. Experimental tests were conducted to analyze the relationship between the measured AUV pressure and the distance, frequency and amplitude of the vibration source. Analysis results demonstrate that the experimental measurements were consistent with simulation results. Based on the relationship between the sensor measurements and the vibration source, a neural network model was used to identify the coordinates, frequency and amplitude of the vibration source, producing an identification accuracy of 93%. Hence, the proposed ALLS is effective for vibration source perception of AUVs.

Keywords: biomimetic sensor, artificial lateral line, vibration source perception, autonomous underwater vehicles, neural networks

(Some figures may appear in colour only in the online journal)

[4] Author to whom any correspondence should be addressed.

1. Introduction

The perception of vibration sources can be used to detect, classify, locate, and track underwater targets and it is of great strategic importance for underwater communication and navigation, ship safeguarding, position monitoring of submarines, underwater weapons and anti-submarine helicopters. Currently, ultrasonic waves, visual images and electromagnetic devices are often used to perceive vibration sources of autonomous underwater vehicles (AUVs) [1]. As a most popular device, sonar can perceive the position of AUV vibration sources and attitudes/positions via radio waves [2]. However, due to the shielding effect of water, radio signals cannot travel far. In complex underwater environments, the performance of sonar with respect to vibration source detection may be decreased. Optics sensors can perceive AUV vibration sources but light phenomena such as refraction and darkness strongly interfere with their applications in motion control, positioning and environmental perception of underwater vehicles. Furthermore, electromagnetic waves are severely attenuated in water [3, 4]. Consequently, current methods using ultrasonic waves, visual images and electromagnetic devices may suffer from low detection accuracy for AUV vibration sources.

Sensing the surrounding vibration sources accurately in complex underwater environments is a challenging task. Inspired by fish laterals, which enable fishes to effectively perform prey tracking, obstacle avoiding, group travel, information exchange, and long-range migration [5–7], a new sensing and navigation positioning technology is proposed, namely, the artificial lateral lines system (ALLS) [8]. ALLS is a promising technique in compensating existing technologies to improve the identification accuracy of underwater vibration sources. However, most current ALLS research focuses on the perception mechanism and biomimetic sensor design [9]. The design of a systematic ALLS that is ready for practical applications is still an unsolved problem.

In order to address the aforementioned issue in ALLS, this paper aims to develop a practicable and applicable ALLS for AUVs. The contributions of this paper are described as follows.

(1) A novel ALLS is developed using high-precision pressure sensors with optimal design of sensor distribution.
(2) A practical AUV experimental device equipped with the proposed ALLS is developed to perform vibration source perception/positioning.

This paper is organized as follows. Section 2 reviews the related work in vibration source perception/positioning of AUVs. In section 3, according to the basic theory of fluid mechanics, a mathematical model is established to locate the AUV vibration sources. The mathematical relationship between the vibration source coordinates and the surface pressure of the lateral line carrier is described. Numerical simulation is carried out in section 4 to investigate the optimal distribution of pressure sensors in the ALLS. The experimental AUV device is introduced in section 5. The characteristics of the ALLS surface pressure caused by vibration sources with different coordinates, frequency and amplitude are analyzed. Section 6 draws the main conclusions.

2. Related work

The lateral lines of fish have been studied in various fields such as biology, neurology and engineering. Fish predation and obstacle avoidance actions are the result of an interaction of multiple sensory organs, such as chemical perception, acoustic perception, and mechanical sideline perception. Fish can also evade danger through taste buds and the olfactory system. It has been discovered that most fish mainly rely on the lateral line system to achieve omni-directional vibration perception, obstacle avoidance, communication, group travel, and target positioning [10–13]. The lateral line system is a sensory system that fish can use to sense water flow and pressure gradients. It consists of thousands of arrays of surface neurons [14]. Each neuron contains several cilia bundles, sealed in a gelatinous shell. Fluids may trigger the neurons to enable fish to identify near-field objects and water currents [15, 16]. Coombs and Conley [17–19] found that the mottled sculpin can always locate vibrating objects. If the surface neurons are removed from one side of the sculpin, the initial positioning angle error may increase from 20° to 60°. As a result, it can be deduced that fish rely mainly on the lateral line system to achieve accurate positioning of vibrating objects. Janssen and Corcoran [20] found that as long as the lateral line system of the mottled sculpin is intact, it can not only determine the direction of the source, but also the distance to the source and the change in vibration intensity. However, the estimated position is limited to short distance (approximately the length of a fish body). Enger *et al* [21] discovered that *Lepomis macrochirus* only reacts strongly to balls with vibration frequency below 10 Hz in a dark environment. Furthermore, Yang *et al* [22] used surface micromachining to manufacture a set of miniaturized hot wire speed sensors (HWAs) to perform dipole source positioning and hydrodynamic wake monitoring. Chen *et al* [23] developed an ALLS for hydrodynamic object tracking whereas the developed system is yet to be used in practice. Yang *et al* [24] designed a carrier with a sensor array using a 3-degree-of-freedom mechanical arm and carried out experiments on tracking and positioning of vibration sources. They also built a corresponding ALLS tester [25]. A PVC pipe (89 mm in diameter) was used to imitate the fish body to study the 3D positioning ability of the ALLS. Good results were obtained in their experiments. McConney *et al* [26] designed a biomimetic hydrogel-covered cilia sensor system through precision casting. The performance of object detection is enhanced by two orders of magnitude [26]. When detecting a 50 Hz dipole source with 15 mm in distance, a speed sensitivity of 2.5 μm s^{-1} was achieved. Mohsen *et al* [27] developed a sensitive artificial ciliary flow sensor, which can be mounted on a miniature membrane with a floating electrode. Simulations were conducted using the developed sensor to detect a 35 Hz dipole source. The position and distance of the underwater dipole source were identified accurately.

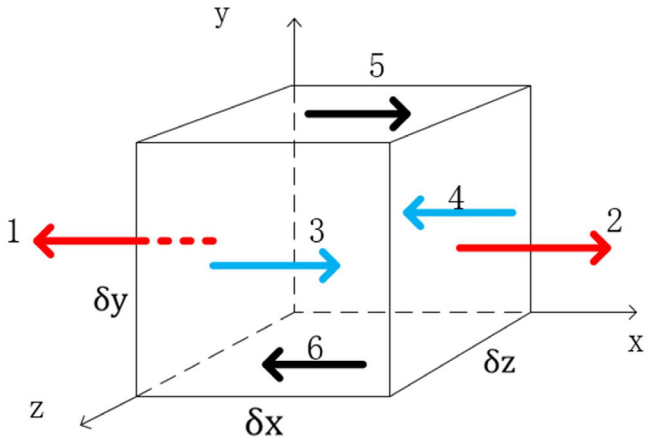

Figure 1. Analysis of the unit volume force.

Most of the existing research on ALLS mainly focuses on theoretical analysis and experimental testing in sensor design, flow velocity perception, vibration source perception and positioning, and obstacle shape recognition. Practical ALLS devices that are suitable for AUVs have not been found yet. This paper will address this concern by developing a novel practical ALLS for AUVs.

3. Hydromechanics of the proposed ALLS

The hydromechanics model of the proposed ALLS assumes that the fluid is incompressible, satisfying the continuity equation, Euler equation, and Navier–Stokes equation. The fluid is also non-viscous and non-rotating, consistent with the potential flow theory.

3.1. Euler equations

When the source vibrates, a force is generated on the surrounding water flow that gives rise to changes in the flow environment [28–30]. Applying Newton's second law to a small volume element in the fluid (see figure 1) we get

$$\delta\vec{F} = \delta m\vec{a} \tag{1}$$

where, in a small volume δA, $\delta\vec{F}$ is the micro force, δm is the volume mass and $\vec{a}$ is the volume acceleration. $\delta\vec{F}$ can be decomposed into orthogonal force components δF_n. (n =1, 2, …, 6). The vertical force components are δF_1 and δF_2. Normal stress and shear stress are expressed as follows:

$$\sigma_n = \lim_{\delta A\to 0}\frac{\delta F_n}{\delta A} \tag{2}$$

$$\tau_1 = \lim_{\delta A\to 0}\frac{\delta F_1}{\delta A} \tag{3}$$

$$\tau_2 = \lim_{\delta A\to 0}\frac{\delta F_2}{\delta A}. \tag{4}$$

Combined with the Taylor series expansion, the force components on the hexahedron can be expressed as follows:

$$\text{Side 1}: (\sigma_{xx} - \frac{\partial\sigma_{xx}}{\partial x}\cdot\frac{\partial x}{2})\delta_y\delta_z$$

$$\text{Side 2}: (\sigma_{xx} + \frac{\partial\sigma_{xx}}{\partial x}\cdot\frac{\partial x}{2})\delta_y\delta_z$$

$$\text{Side 3}: (\tau_{zx} + \frac{\partial\tau_{zx}}{\partial z}\cdot\frac{\partial z}{2})\delta_x\delta_y$$

$$\text{Side 4}: (\tau_{zx} - \frac{\partial\tau_{zx}}{\partial z}\cdot\frac{\partial z}{2})\delta_x\delta_y$$

$$\text{Side 5}: (\tau_{zx} + \frac{\partial\tau_{yx}}{\partial y}\cdot\frac{\partial y}{2})\delta_x\delta_z$$

$$\text{Side 6}: (\tau_{zx} - \frac{\partial\tau_{yx}}{\partial y}\cdot\frac{\partial y}{2})\delta_x\delta_z$$

where δ_x, δ_y and δ_z are the normal stress in the x, y and z directions, σ_{xx} is the component of ∂x in the x direction, τ_z is the shear stress in the z direction, and τ_{zx} is the component of τ_z in the x direction.

The balanced expressions of forces in the x-axis, y-axis, and z-axis are

$$\delta F_{sx} = (\frac{\partial\sigma_{xx}}{\partial x} + \frac{\partial\tau_{yx}}{\partial y} + \frac{\partial\tau_{zx}}{\partial z})\delta_x\delta_y\delta_z \tag{5}$$

$$\delta F_{sy} = (\frac{\partial\tau_{xy}}{\partial x} + \frac{\partial\sigma_{yy}}{\partial y} + \frac{\partial\tau_{zx}}{\partial z})\delta_x\delta_y\delta_z \tag{6}$$

$$\delta F_{sz} = (\frac{\partial\tau_{xz}}{\partial x} + \frac{\partial\tau_{yz}}{\partial y} + \frac{\partial\sigma_{zz}}{\partial z})\delta_x\delta_y\delta_z. \tag{7}$$

The resultant forces of the hexahedron may be expressed as follows:

$$\delta\vec{F}_s = \delta m\cdot\vec{a} = \delta F_{sx}\hat{i} + \delta F_{sy}\hat{j} + \delta F_{sz}\hat{k} \tag{8}$$

$$\delta\vec{F} = \delta m\cdot\vec{a} = \rho(\frac{\partial\vec{V}}{\partial t} + \vec{V}\cdot\nabla\vec{V})\delta_x\delta_y\delta_z \tag{9}$$

where ρ is the volume density, $\hat{i}$, $\hat{j}$ and $\hat{k}$ are unit vectors in the x, y and z directions, respectively, $\vec{V}$ is the speed vector, $\frac{\partial\vec{V}}{\partial t}$ is the time-varying acceleration, and $\vec{V}\cdot\nabla\vec{V}$ denotes the convection acceleration. Supposing that the gravity has a component g_x in the x direction, we derive

$$\rho g_x + \frac{\partial\sigma_{xx}}{\partial x} + \frac{\partial\tau_{yx}}{\partial y} + \frac{\partial\tau_{zx}}{\partial z} = \rho(\frac{\partial u}{\partial t} + u\frac{\partial u}{\partial x} + v\frac{\partial u}{\partial y} + w\frac{\partial u}{\partial z}) \tag{10}$$

$$\rho g_y + \frac{\partial\tau_{xy}}{\partial x} + \frac{\partial\sigma_{yy}}{\partial y} + \frac{\partial\tau_{zx}}{\partial z} = \rho(\frac{\partial v}{\partial t} + u\frac{\partial v}{\partial x} + v\frac{\partial v}{\partial y} + w\frac{\partial v}{\partial z}) \tag{11}$$

$$\rho g_z + \frac{\partial\tau_{xz}}{\partial x} + \frac{\partial\tau_{yz}}{\partial y} + \frac{\partial\sigma_{zz}}{\partial z} = \rho(\frac{\partial w}{\partial t} + u\frac{\partial w}{\partial x} + v\frac{\partial w}{\partial y} + w\frac{\partial w}{\partial z}) \tag{12}$$

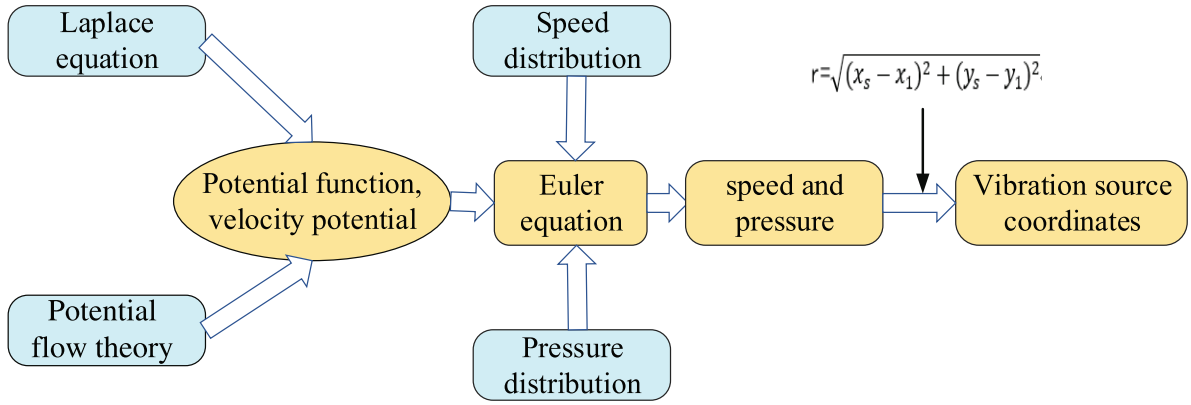

Figure 2. Mathematical model derivation flow chart.

where u, v, and w are the three directions of the fluid. In non-viscous fluid, there is no shear stress, only normal stress. The vector expression is as follows:

$$\sigma_{xx} = \sigma_{yy} = \sigma_{zz} = -p. \tag{13}$$

Combining equations (10)–(13) yields

$$\rho\vec{g} - \nabla p = \rho[\frac{\partial \vec{V}}{\partial t} + (\vec{V}\cdot\nabla)\vec{V}] \tag{14}$$

where Δp denotes the pressure gradient, $[\frac{\partial \vec{V}}{\partial t} + (\vec{V}\cdot\nabla)\vec{V}]$ represents the acceleration and $\mu\nabla^2\vec{V}$ represents the viscous force. Equation (14) is the Euler equation in the ideal fluid while for practical problems the viscous fluids are often used. Equation (14) can be rewritten for viscous fluids by adding a viscous force term according to the Navier–Stokes equations (3):

$$\rho\vec{g} - \nabla p + \mu\nabla^2\vec{V} = \rho(\frac{\partial \vec{V}}{\partial t} + \vec{V}\cdot\nabla\vec{V}) \tag{15}$$

where $\mu\nabla^2\vec{V}$ is the viscous force term.

3.2. Plane potential flow theory

An incompressible, non-rotating ideal flow is called a potential flow. Its potential function satisfies the Laplace equation in equation (16):

$$\nabla^2\varphi = 0 \tag{16}$$

where φ is the potential function. There is no shear stress in the ideal fluid. The fluid microcell can only slide along but cannot pass through the surface of the object. Therefore, the impenetrable condition is satisfied.

$$\upsilon \cdot n = v_b \cdot n \tag{17}$$

where υ denotes the fluid velocity, v_b denotes the speed of the object, and n denotes a normal vector.

$$\frac{\partial\varphi}{\partial n} = v_b \cdot n. \tag{18}$$

According to the boundary conditions of the object, the potential function can be obtained in a complex water area. Let us assume the source coordinates of the vibration dipole (x_0, y_0), point coordinates $(x_0 + \delta_{x_0}, y_0)$. The dipole potential function can be expressed as

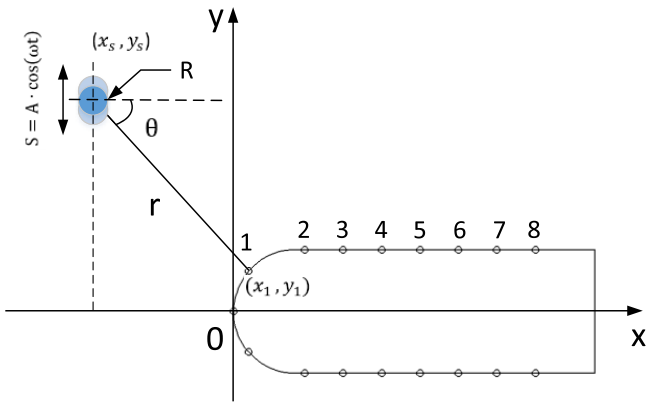

Figure 3. Vibration source positioning diagram.

$$\varphi = \frac{m}{4\pi}\ln\left\{(x-x_0)^2 + (y-y_0)^2\right\} - \frac{m}{4\pi}\ln\left\{(x-(x_0+\delta_{x_0}))^2 + (y-y_0)^2\right\}. \tag{19}$$

When $(\delta_{x_0} \to 0)$, the potential function can be simplified to

$$\varphi = \frac{M}{2\pi}\frac{x-x_0}{(x-x_0)^2 + (y-y_0)^2}. \tag{20}$$

3.3. Mathematical model of the positioning

Figure 2 shows the working flow diagram of vibration source location. First, the potential function and velocity potential are obtained according to the Laplace equation and potential flow theory. Then the relationship between speed and pressure is obtained by the Euler equation. Lastly, the coordinates of the vibration source can be calculated by solving the Laplace equation.

Figure 3 depicts the mathematical model of vibration source positioning. When a ball vibrates in an ideal fluid, the vibration of the object will continuously influence the surrounding fluid that, causing the flow of the fluid. However, the energy is limited. The fluid movement is mainly concentrated in the water area near the vibrating object [28, 29].

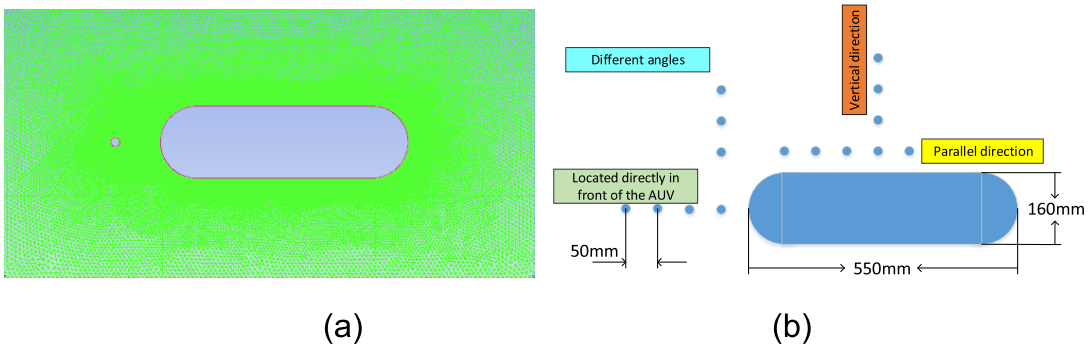

Figure 4. (a) The simulation model; (b) the simulation settings.

The instantaneous displacement of the ball vibration can be expressed as [30, 31]

$$S = A \cdot \cos(\omega t). \tag{21}$$

The instantaneous speed of the ball is

$$u = A \cdot \omega \cdot \sin(\omega t). \tag{22}$$

The Laplace equation has a solution $1/r$, where r is the distance to the origin. When the ALLS is away from the vibration source, the general form of the solution to the Laplace equation may be expressed as

$$\varphi = -\frac{a}{r} + Q \cdot \nabla \frac{1}{r} + \cdots \tag{23}$$

where a is a constant (because the flow of incompressible fluid through any closed surface should be zero, $a = 0$) and $Q = uR^3/2$, where u and R denote the speed and radius of the vibration source, respectively. Therefore, the potential function can be expressed in equation (24):

$$\varphi = -\frac{R^3}{2r^2} \cdot u \cdot n \tag{24}$$

where n denotes the normal vector of the direction of motion of the vibration source, which can be approximated by $\cos\theta$, and $u = A \cdot \omega \cdot \sin(\omega t)$. Hence, the potential function can be further expressed as

$$\varphi = -\frac{R^3}{2r^2} \cdot A \cdot \omega \cdot \sin(\omega t)\cos\theta \tag{25}$$

$$\frac{\partial \varphi}{\partial t} = -\frac{R^3}{2r^2} \cdot A \cdot \omega^2 \cdot \cos(\omega t)\cos\theta. \tag{26}$$

Since $r\cos\theta = x_s - x_1$, $r = \sqrt{(x_s - x_1)^2 + (y_s - y_1)^2}$, and $S = A \cdot \cos(\omega t)$, we can obtain

$$\frac{\partial \varphi}{\partial t} = -\frac{R^3 S\omega^2}{2} \cdot \frac{x_s - x_1}{((x_s - x_1)^2 + (y_s - y_1)^2)^{\frac{3}{2}}}. \tag{27}$$

In an arbitrary vector field with zero rotation, the velocity caused by the potential flow can be described by a scalar gradient. Substituting $v = \Delta\varphi$ into the Euler equation yields

$$\frac{\partial v}{\partial t} + \frac{1}{2}\nabla v^2 - v \times \mathrm{rot} v = -\frac{p}{\rho}. \tag{28}$$

Equation (28) can be rewritten as

$$\frac{\partial \varphi}{\partial t} + \frac{v^2}{2} + \frac{p}{\rho} = f(t) \tag{29}$$

where $f(t)$ is an arbitrary function of time. Since velocity is equal to the derivative of the potential function with respect to the coordinates, φ may vary with time. If $f(t) = 0$, then the distribution of pressure in the flow field becomes

$$p = p_0 - \frac{\rho v^2}{2} + \rho\frac{\partial \varphi}{\partial t} \tag{30}$$

where p_0 is the pressure at infinity point in the flow field. If the flow is a potential flow and the fluid is incompressible, the velocity of the water flow caused by the vibration is very small (i.e. $\frac{\partial \varphi}{\partial t} \gg v^2$). Thus, the squared term $\frac{\rho v^2}{2}$ in equation (30) can be ignored. The formula for the pressure and velocity of the sensor at a distance r is then expressed as

$$p = \rho\frac{R^3 S\omega^2}{2} \cdot \frac{x_s - x_1}{((x_s - x_1)^2 + (y_s - y_1)^2)^{\frac{3}{2}}} \tag{31}$$

where (x_1, y_1) is the sensor coordinate.

4. Numerical simulation

4.1. The establishment of the simulation model

The FLUENT software is used to implement the simulation. Figure 4 shows the simulation model. The simulation area is set to 2000 × 1200 mm as illustrated in figure 4(a). The simulation model is 550 mm in length and 160 mm in diameter. The mesh types are triangular meshes and the solver type is based on pressure. The operating pressure is 10 325 Pa, the gravity acceleration is 9.8 N kg^{-1}, the velocity-inlet size is set to zero, and the pressure-outlet is set to zero.

As illustrated in figure 4(b), the omni-directional perception of the lateral carriers is enabled by setting the vibration source to four different positions in the simulation. These four positions are located directly in front of the lateral line carriers at different angles from the lateral line carriers, perpendicular to the lateral line carriers or parallel to the lateral line carriers.

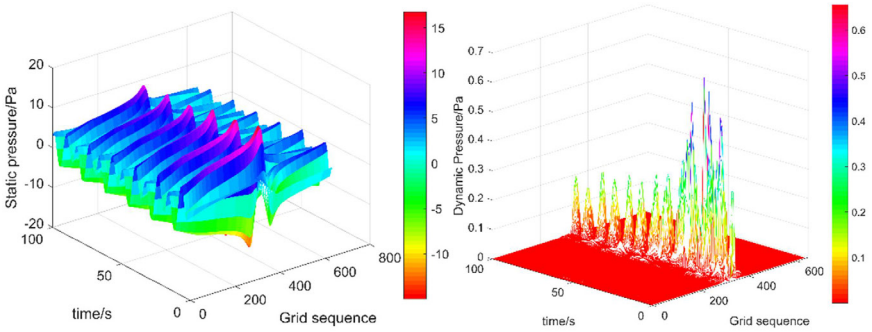

(a)

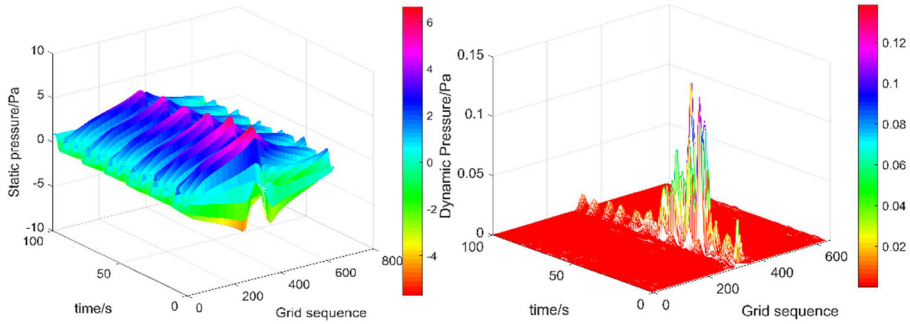

(b)

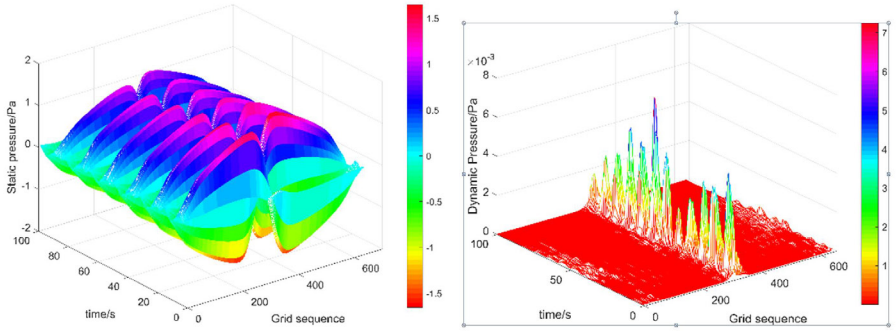

(c)

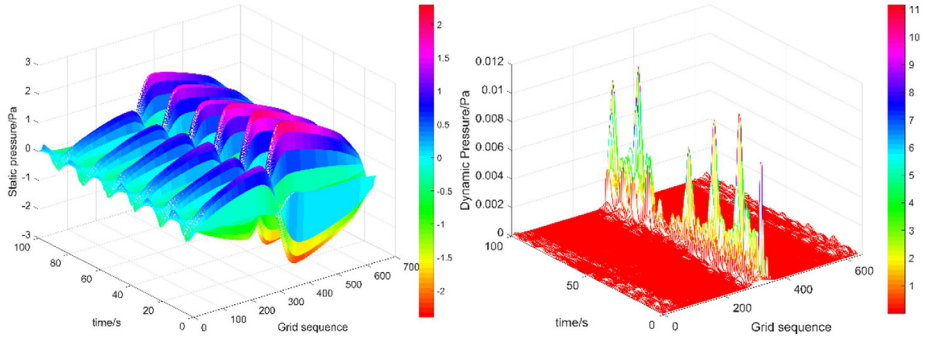

(d)

Figure 5. (a) 50 mm in front of the carrier; (b) 100 mm in front of the carrier; (c) 200 mm in front of the carrier; (d) 300 mm in front of the carrier.

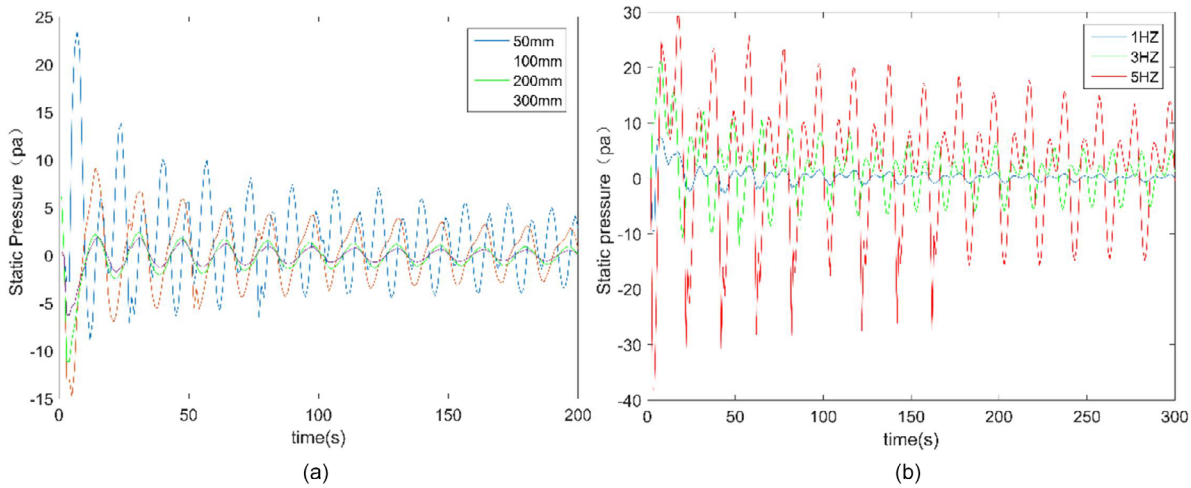

Figure 6. (a) The relationship between distance and pressure; (b) the relationship between frequency and pressure.

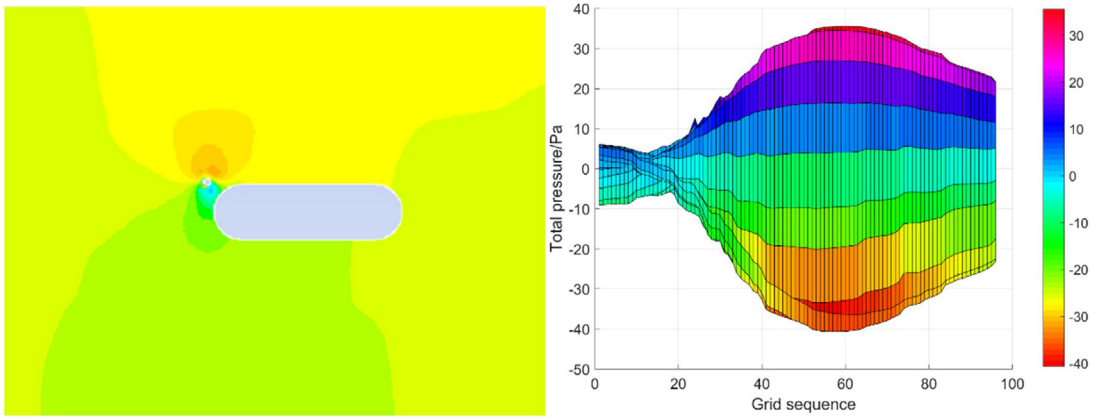

Figure 7. The vibration source is at 45° with the center of the ball head.

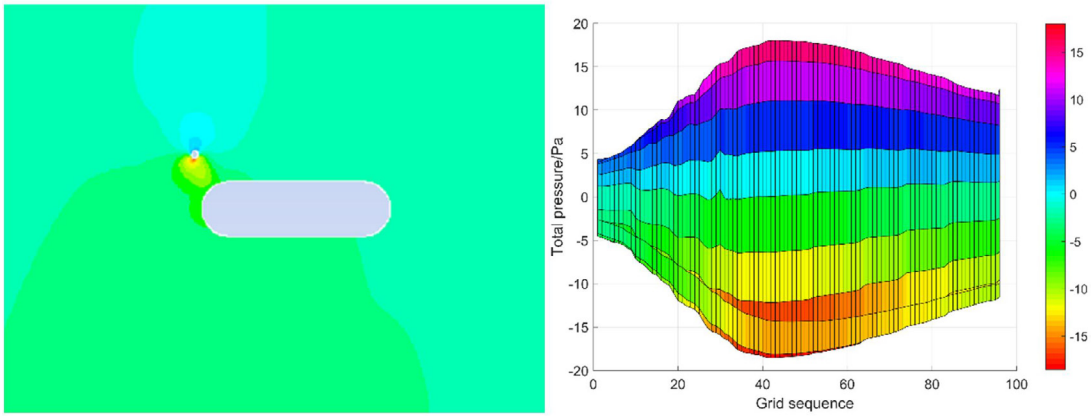

Figure 8. The vibration source is at 56.31° with the center of the ball head.

4.2. Simulation results

4.2.1. The vibration source is located directly in front of the ALLS carrier. Figure 5 illustrates the simulation results of the dynamics and the static pressures that are perceived by a lateral line carrier at a certain frequency and varying distances. The x-axis denotes the time, the y-axis denotes the grid sequence, and the z-axis denotes the pressure variations.

The pressure variations at different positions, 50, 100, 200 and 300 mm in front of the carrier were analyzed. Figure 6 shows the analysis results. As can be seen in figure 6(a), the pressure variations on the left and right sides exhibit a certain symmetry, and the distance is inversely proportional to the pressure. In figure 6(b), the pressure is proportional to the vibration frequency.

According to the simulation results, the dynamic pressure is almost zero, and hence it can be ignored here. The static pressure can approximate the total pressure. The total pressure data is the actual pressure measured by the sensor during the experiment. Therefore, only the total pressure is analyzed below.

4.2.2. Analysis from different angles to ALLS carriers. Figures 7 and 8 show the analysis results of the surface pressure variations from different angles to the ALLS carriers. When the vibration source is located at 45° with the center of the ball head, the extreme point of the pressure appears at the 58th grid sequence in figure 7. The computed angle is $\theta = 48.44°$, which is 3.44° greater than the true value of 45°. Similarly, as depicted in figure 8, when the vibration source is at 56.31°, the computed angle is 59.61°. These results demonstrate that when the vibration source is at a certain angle with the lateral line carrier, the general orientation of the stimulation signal can be determined by the distribution point of the maximum pressure of the ball head.

4.2.3. Parallel to ALLS carriers. Figure 9 shows the analysis results of the pressure distribution when the vibration sources are parallel to the ALLS carriers. In figure 9(a), at the distance of 100 mm ahead of the ALLS carriers the extreme pressure point corresponds to the 383th grid node while for a 150 mm distance it corresponds to the 330th grid node in figure 9(b). When the distance is 200 mm, the extreme pressure point corresponds to the 280th grid node in figure 9(c). The extreme pressure point in figure 9(e) corresponds to the 180th grid node. As a result, when the vibration source moves parallel along the carrier, the grid node corresponding to the extreme pressure point will decrease with increasing distance.

4.2.4. Perpendicular to ALLS carriers. Figure 10 illustrates the analysis results of the pressure distribution when the vibration sources are perpendicular to ALLS carriers. In the simulation, the distance is varied with constant frequency. As can be seen in figure 10, the pressure perceived by the lateral line carrier is inversely proportional to the distance.

In summary, the surface pressure distribution characteristics of the ALLS carriers can be obtained through simulation analysis. The distance between the vibration source and the carrier is inversely proportional to the perceived pressure, and the vibration frequency is proportional to pressure. These results demonstrate that the carriers are able to sense the pressure signals and the intensity changes in specific directions.

5. Experimental

5.1. Experimental setup

The ALLS carrier, as illustrated in figure 11, was designed and manufactured to implement the experimental tests in this study. Twenty-five high-precision pressure sensors (MS5803-07BA) were selected and installed in the carrier. These pressure sensors were sealed to the housing, and a battery and a microcontroller were imbedded inside the carrier. The inside devices were connected to the outside through a watertight connector. The whole system was sealed with O-rings.

Figure 12 describes the carrier in detail. The entire system was driven by a 12 V lithium battery. The supply voltage to each sensor was 3.3 V. The microcontroller transmitted the data to the signal processing system through the TTL-232 cable. The signal processing system was programmed using C# language to receive and store pressure data in real time. The acquisition frequency was 12 Hz. The experimental platform is illustrated in figure 13. The size of the pool was $2000 \times 1500 \times 1200$ mm. The water-depth was 1000 mm, the water temperature was 13 °C, and the atmospheric pressure was 1.01×10^5 Pa. Table 1 lists the experimental parameter settings.

5.2. The experimental results

The pressure measured by the sensor was affected by many uncontrollable factors that included, but were not limited to, the variations in the weather, altitude, temperature, water depth, and also sensor hardware [32–34]. The true pressure change was depicted through the discrepancy between the sensor measured pressure and the hydrostatic pressure. The measurements of the 25 pressure sensors in the water are illustrated in figure 14.

Since the measurements of the sensors presented slight fluctuations, a filtering processing was applied to the sensory signals. Figure 15(a) shows the pressure waveform of sensor No. 25 at the front end of the carrier. Figure 15(b) shows the frequency spectrum of the pressure using fast Fourier transform. It can be observed that the frequency spectrum of the pressure is corrupted by noise and there are few significant amplitude characteristics. Figure 15(c) shows the filtered signal, where the noise has been effectively depressed.

Figure 16 illustrates the pressure distribution of the 25 sensors. The extreme pressure point appeared at 13 s on sensor No. 25, which was installed in front of the carrier. The maximum pressure was ±80 Pa. The pressure fluctuations of the other 24 sensors were within the range of ±30 Pa.

A comparison analysis between the simulation and experimental data is depicted in figure 17 when the vibration source frequency is 3 Hz. Certain similarities can be observed between the simulation and experimental results. The maximum, minimum, mean and kurtosis of the experimental result are respectively 18 Pa, 81 Pa, 53.7 Pa and 2.7 while for the simulation result they are 3.5 Pa, 81.1 Pa, 52.3 Pa and 2.1. Hence, the statistics of the experimental data are close to those calculated from the simulation data. However, due to sensor and background noise the degree of variation of the experimental curve is more severe than that of the simulation curve.

5.2.1. Relationship between pressure and frequency. When the vibration source was located at 50 mm in front of the carrier, the amplitude was 10 mm and the frequencies were 1, 3 and 5 Hz, respectively. The data fitting was applied to the measurement of sensor No. 25. Figure 18 compares the data fitting results of the experimental and the simulation results. The obtained data fitting functions are

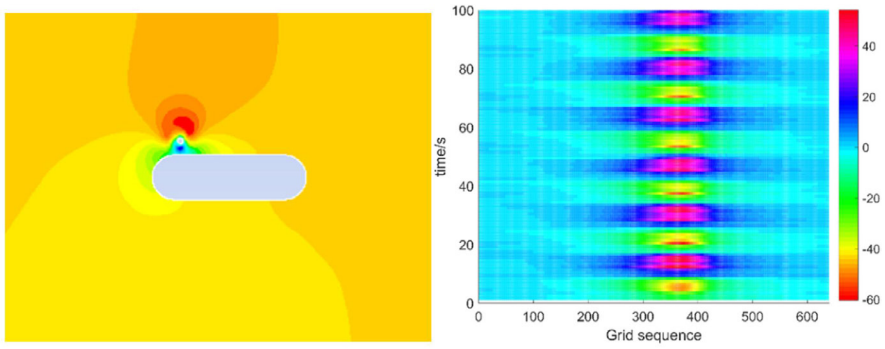

(a)

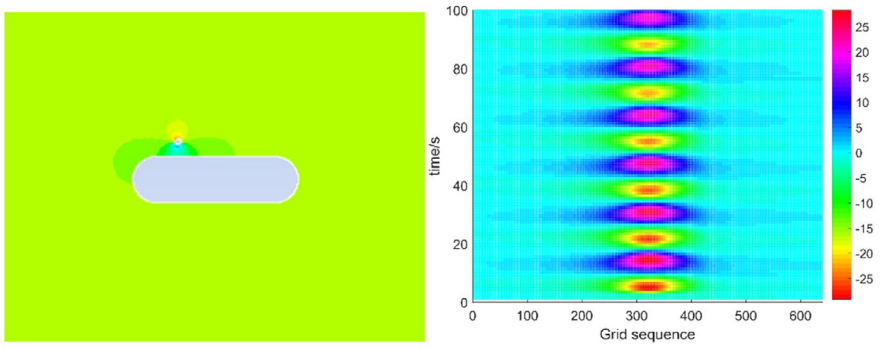

(b)

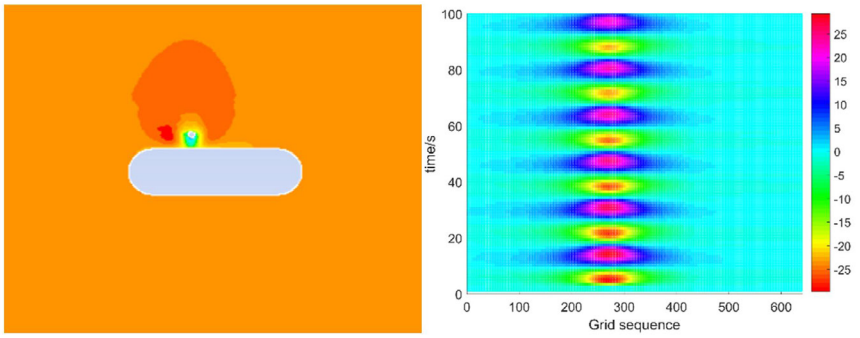

(c)

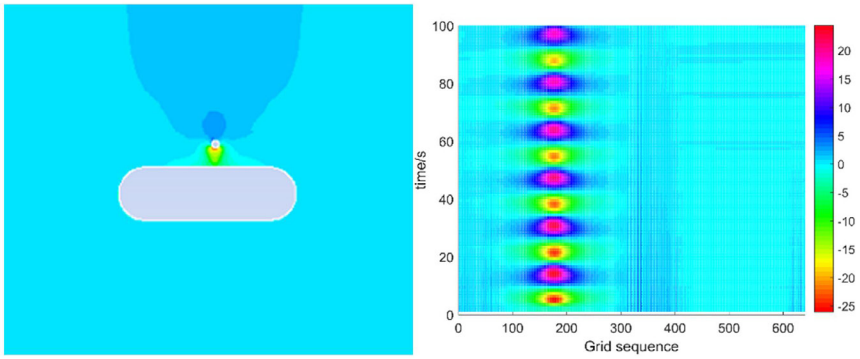

(d)

Figure 9. Pressure distribution at different distances: (a) 100, (b) 150, (c) 200, and (d) 300 mm.

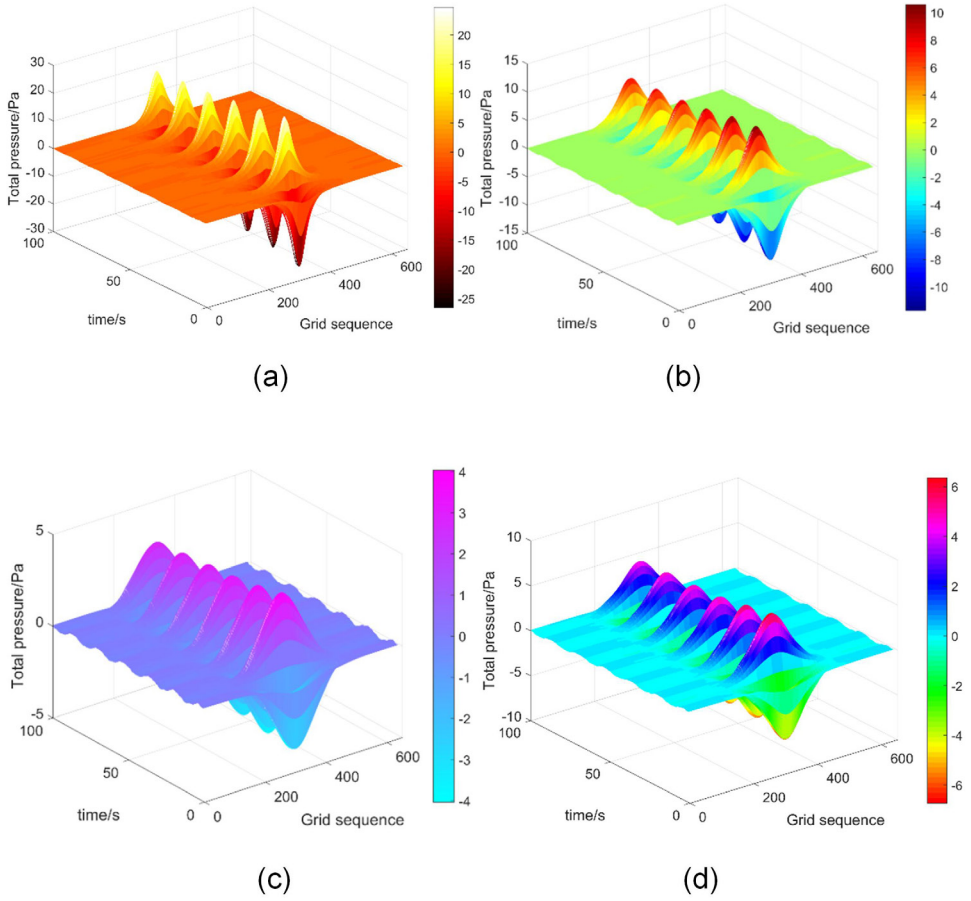

Figure 10. Pressure distribution at different distances: (a) 50, (b) 100, (c) 150, and (d) 200 mm.

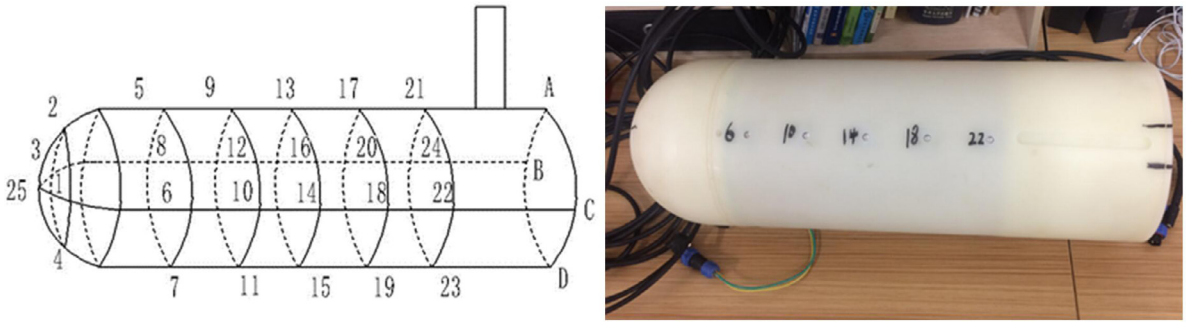

Figure 11. Sensor layout and lateral line carrier physical map.

$$p_e = -2\omega^2 + 30.5\omega - 10.5 \tag{32}$$

$$p_s = -1.25\omega^2 + 28.5\omega - 1.25 \tag{33}$$

where p_e indicates the pressure of the experimental data, p_s indicates the pressure of the simulation data, and ω indicates the vibration frequency.

As can be seen in figure 18, the simulated pressure is larger than the experimental one. The pressure on the surface of the carrier increases with frequency. Because the experiment test was conducted with low vibration frequencies, the sensor measurement may be subject to sensor and background noise. After noise filtering, the sensor measured value can be smaller than the simulated value.

Nevertheless, the pressure is directly proportional to the frequency of the vibration source. Thanks to the data fitting, the mathematical relationship between the pressure and the frequency at a certain distance is obtained. The maximum pressure can then be used to estimate the source vibration frequency.

5.2.2. Relationship between pressure and distance. The pressure change on the carrier surface was analyzed when the vibration source (10 mm and 3 Hz) was in the vertical

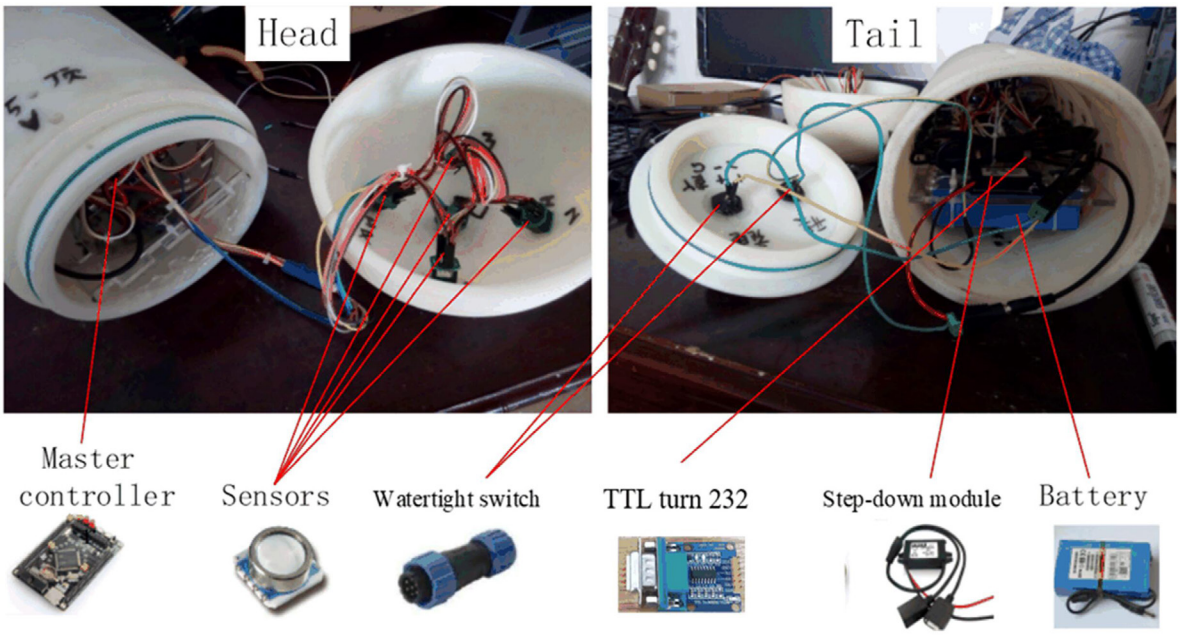

Figure 12. The physical hardware connection of the lateral line.

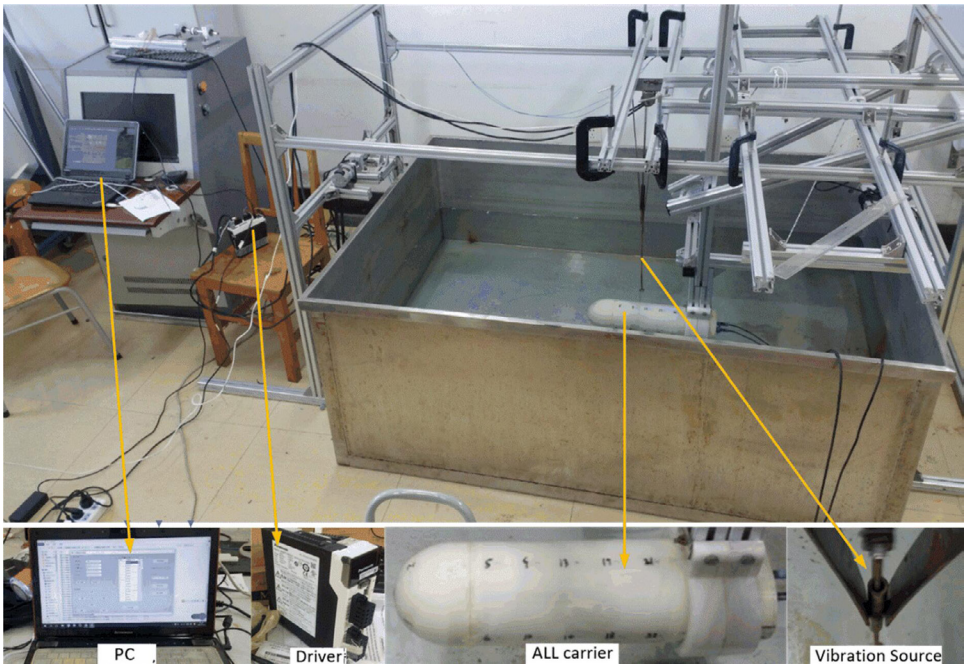

Figure 13. The designed experimental platform.

Table 1. Experimental parameter settings.

Test items	Parameter
Frequency (Hz)	1; 3; 5
Amplitude (mm)	10; 20
Distance (mm)	50; 100; 150; 200

direction of the carrier. Figure 19 shows the relationships between pressure and distance. The data fitting functions of the experimental and the simulation results are

$$P_e = -0.000205d^3 + 0.0389d^2 - 2.68d + 86.19 \quad (34)$$

$$P_s = -0.000126d^3 + 0.0247d^2 - 2.15d + 98.67. \quad (35)$$

The pressures in the experiment and the simulation decrease with increasing distance in figure 19. It is evident that the effective range for identifying the vibration source by an underwater vehicle equipped with an ALLS is limited. The experimental carrier may only sense the range within 0–2 BL (the length of the lateral line carrier) for very low frequency of the vibration sources. However, the sensing range may increase for large vibration frequency because the pressure is proportional to the frequency of the vibration sources.

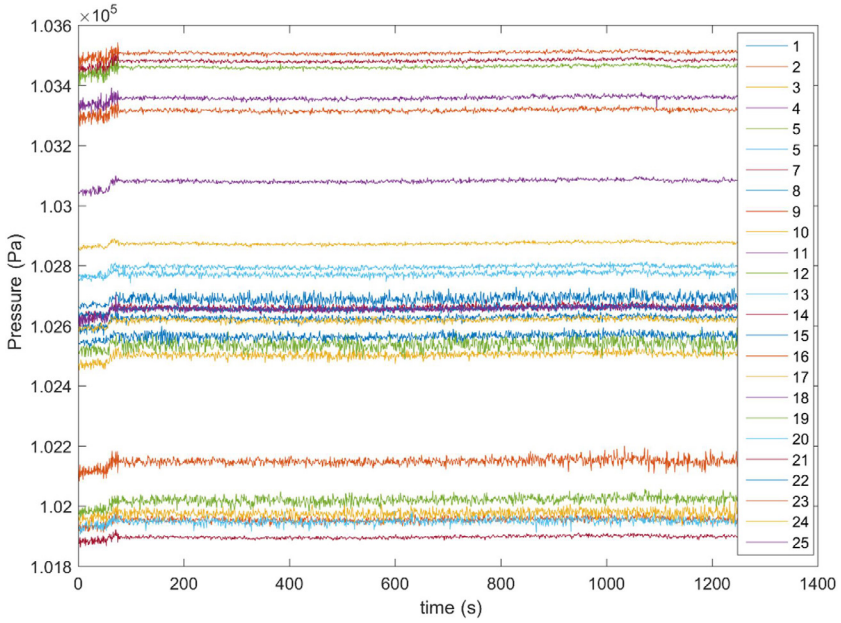

Figure 14. Original signals of the pressure sensor.

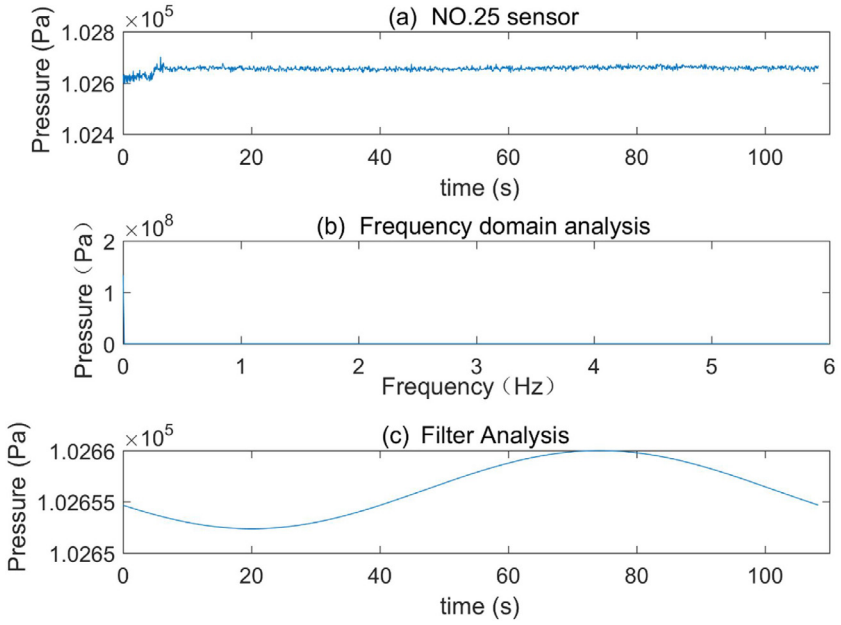

Figure 15. The process of sensor No. 25 pressure data.

5.3. Theoretical verification based on experimental data

Taking the front end of the lateral line carrier as the coordinate origin (0, 0), the coordinate (−20, 0) of the vibration source was selected to discuss the connections between the theoretical and experimental results. Three sensors at different positions were used in the discussion: sensor No. 25 at (0, 0), sensor No. 3 at (23.5, −56.23), and sensor No.1 at (23.5, −56.23). If the data is fed into equation (31), the theoretical coordinate (−18.28, 8.21) of the vibration source can be calculated. The results show that the x-axis coordinate error was 1.72 mm (error rate is 8.6%) while the y-axis error is huge. The reason for this large error in the y direction is probably that the theoretical formula is derived from the ideal fluid, which is incompressible and conforms to the non-rotational flow of the potential flow theory, while in a real experimental environment the fluid will not be ideal. The theoretical formula can only determine the approximate orientation (1D coordinates) and intensity of the vibration source, such as sensing the stimulus signal and the approximate distance and intensity at a certain part of the carrier body (head, torso, tail, etc). At this point, the lateral line carrier already has the ability to sense the orientation and intensity of the stimulus signal.

5.4. Vibration source identification

In order to achieve accurate positioning and localization, neural network learning is employed. Since the concept of

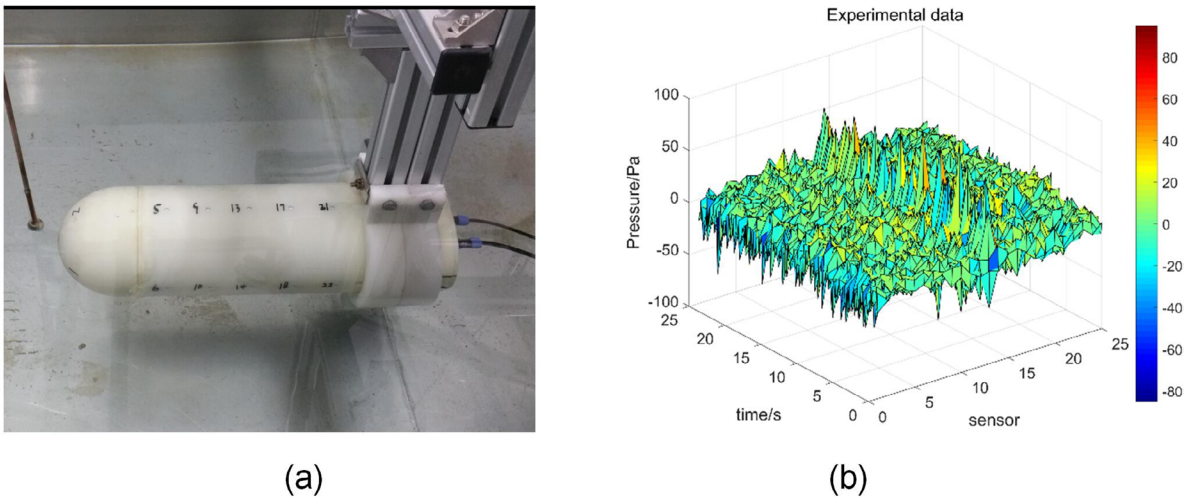

Figure 16. (a) The carrier experiment and (b) the pressure distribution.

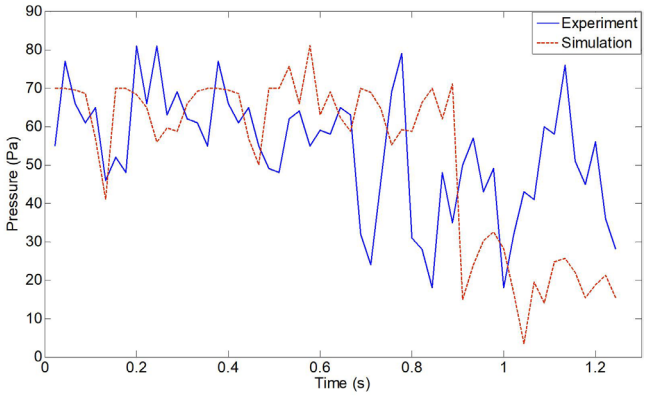

Figure 17. Comparison of experimental and simulation data.

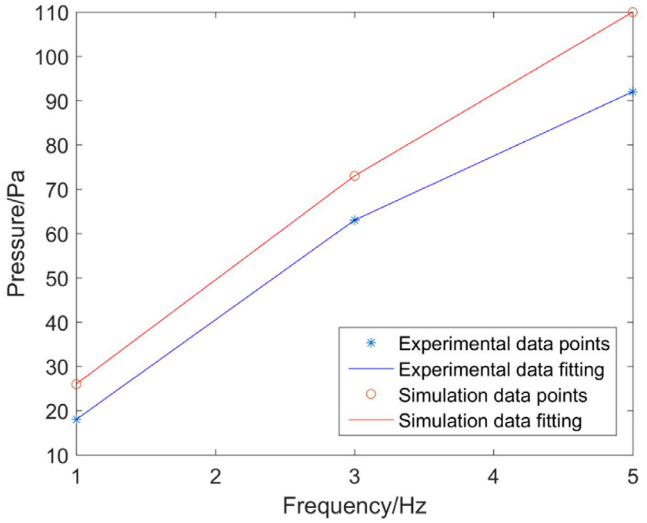

Figure 18. The relationship between pressure and frequency.

an artificial neural network (ANN) has been proposed, it has been rapidly developed and widely used in many applications [35]. In this paper, the ANN learning method is used to realize

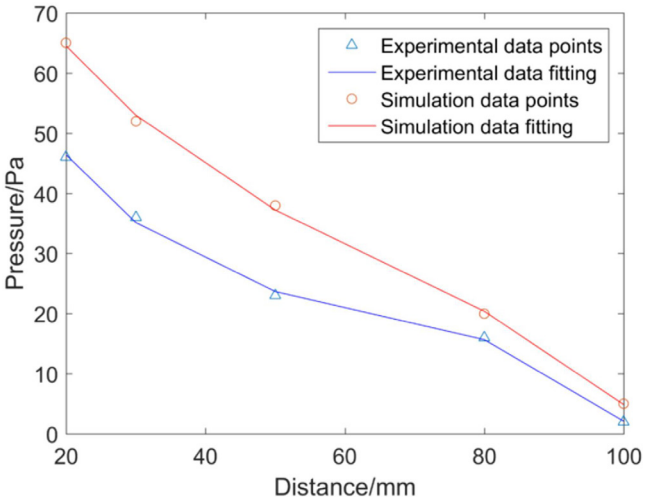

Figure 19. The relationship between pressure and distance.

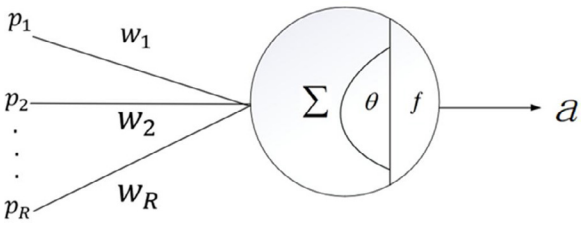

Figure 20. Artificial neuron model.

accurate perception of the coordinates, frequency and amplitude of the vibration source [36].

The ANN model is implemented by simulating the human brain, such as the nonlinear network structure of the simulated nervous system, as shown in figure 20. The artificial neuron is the basic unit of an ANN model, and its function is to realize multiple input values corresponding to a single output value. In figure 20, $p = [p_1, p_2, \ldots, p_R]^T$ is the output vector of the neuron, $w = [w_1, w_2, \ldots, w_R]$ is the weight vector, and θ is the

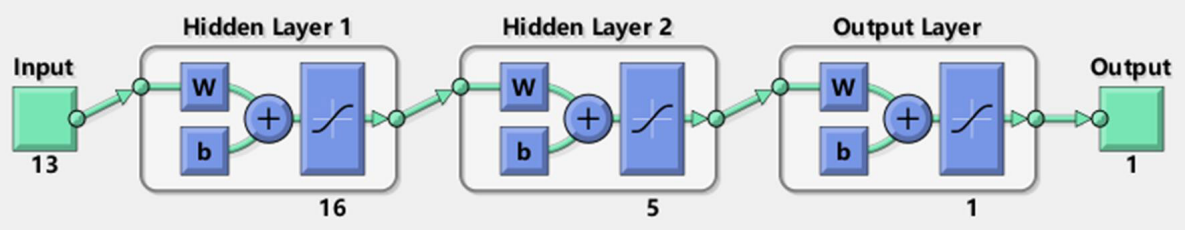

Figure 21. The network topology.

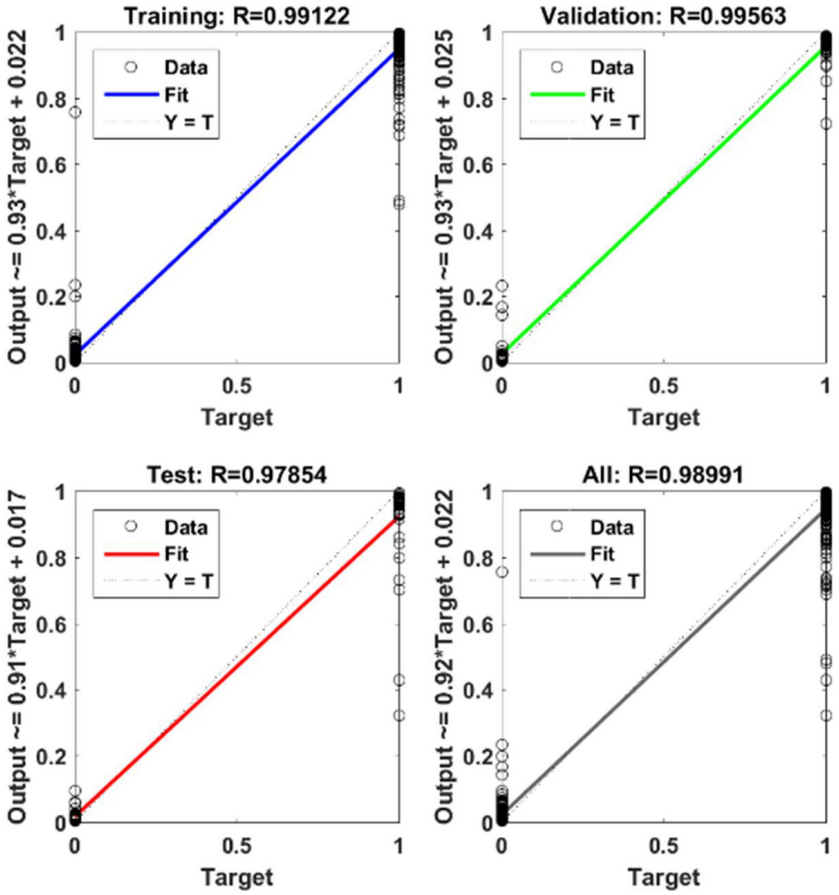

Figure 22. Regression analysis of the training results.

threshold of the neuron. If the weighted sum of the neuron input vector is greater than θ, then the neuron is activated.

In this research, ANN was used to identify the coordinates of the vibration source, the amplitude, and the vibration frequency. The mean square error performance analysis was conducted using the network topology (see figure 21), where w indicates the weight, b indicates the offset, and ~ indicates the activation function.

Experimental data were used for the training, verification and testing of the ANN model. The training, verification and test of the experimental data have all reached a level of 0.97, as depicted in figure 22. The identification accuracy of the vibration frequency was 98.93%, as shown in figure 23(a). The accuracy of the amplitude recognition reached 98.33%, as shown in figure 23(b). The accuracy of the recognition of the coordinates reached 98.93%, as shown in figure 23(c). In this paper, three different coordinates of the vibration source were trained. The best positioning accuracy of the vibration source was obtained when the vibration source was perpendicular to the carrier. The results indicate that the lateral line of the linear array sensor is most sensitive to vibration sources.

When the characteristic parameters (frequency, position and amplitude) of the vibration sources change, the pressure of the lateral line surface carrier changes accordingly. Through the training and computational intelligence of the

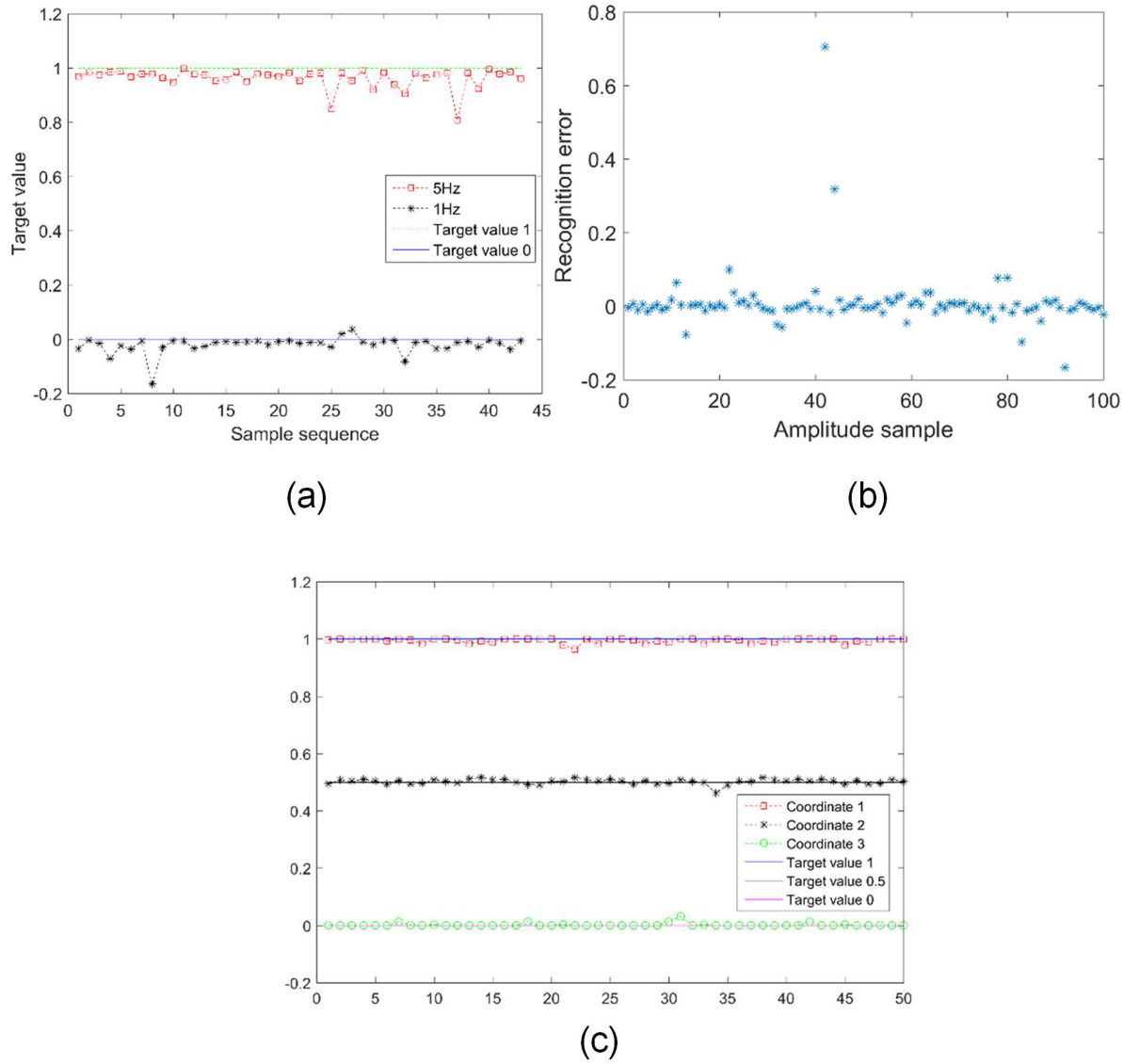

Figure 23. (a) Frequency identification, (b) amplitude identification, and (c) coordinate identification.

ANN algorithm, it becomes possible to achieve accurate recognition of vibration sources.

6. Conclusion and future work

In this research work, a prototypical topology of an ALLS is developed for underwater vehicles. The ALLS was designed and fabricated to successfully identify the coordinates, amplitudes, and frequencies of underwater vibration sources. The relevant mathematical model was established based on the principles of fluid mechanics, and the subsequent mathematical model was established as a relationship between the pressure and the characteristic parameters of the vibration sources.

The technology of fluid simulation enabled the analysis of the pressure changes caused by the position of the vibration source, the frequency, and also the amplitude. There follows a summary of the variation rules pertaining to the ALLS carrier's surface pressure. When the vibration frequency and amplitude are constant, the distance from the vibration source to the carrier is inversely proportional to the pressure perceived by the carrier. The position of the grid node that corresponds to the maximum pressure on the surface of the carrier is consistent with the horizontal coordinates of the vibration source. An azimuth of the vibration source may be determined by the location of the pressure maximum point. Moreover, it is shown that the lateral line carrier may detect changes in the vibration source position.

The mathematical relationship between pressure and the distance to the vibration source, the pressure and vibration frequency may be summed up through the application of the neural network learning algorithm. The algorithm also identifies the characteristic parameters of the vibration source:

(1) Frequency identification: the maximum recognition accuracy was reached at 96.34%.
(2) Amplitude identification: the ANN model recognized the amplitude characteristics (10 mm & 20 mm) of the vibration source with an accuracy of 98.33%.
(3) Coordinate identification: the recognition accuracy rate was over 93%. The best accuracy of 98.93% for the coordinate recognition was obtained when the vibration

source was perpendicular to the direction of the artificial lines.

The analysis results of this research also suggest that it may be helpful in improving the identification accuracy using vibration source sensing and flow field sensing in the underwater vehicles. The developed ALLS may have practical applications in underwater vehicles as well as deep-sea applications.

Future research will include (1) position tracking of the moving vibration sources; (2) new vibration source identification algorithms such as beamforming algorithms, genetic algorithms and least squares; and (3) perception of middle and long distances. Furthermore, although the MS5803-07BA sensor has excellent long-term stability, it is limited by accuracy, acquisition frequency and measurement range. We will consider sensors with higher precision and acquisition frequency in future.

Acknowledgments

This research was supported by the National Natural Science Foundation of China (Grant No. 61540010 & 51505475), Shandong Provincial Natural Science Foundation, China (Grant No. ZR201709240210) and UOW VC Fellowship.

ORCID iDs

Zhixiong Li https://orcid.org/0000-0002-7265-0008

References

[1] Thomson M, Dosso E and Barclay R 2017 Modeling AUV localization error in a long baseline acoustic positioning system *IEEE J. Ocean. Eng.* **99** 1–14
[2] Paull L, Saeedi S, Seto M and Li H 2014 AUV navigation and localization: a review *IEEE J. Ocean. Eng.* **39** 131–49
[3] Chen Y, Zheng D, Miller A and Farrell J A 2013 Underwater inertial navigation with long base line transceivers: a near-real-time approach *IEEE Conf. Decis. Control* **2** 5042–7
[4] Xiao G, Wang B, Deng Z, Fu M and Ling Y 2017 An acoustic communication time delays compensation method for master-slave AUV cooperative navigation *IEEE Sens. J.* **17** 504–13
[5] Fan Z, Chen J, Zou J, Li J, Liu C and Delcomyn F 2002 Development of artificial lateral-line flow sensors *Solid-State Sensor, Actuator and Microsystems Workshop*
[6] Schwalbe A, Bassett K and Webb F 2012 Feeding in the dark: lateral-line-mediated prey detection in the peacock cichlid *Aulonocara stuartgranti J. Exp. Biol.* **215** 2060
[7] Xu Y and Mohseni K 2017 A pressure sensory system inspired by the fish lateral line: hydrodynamic force estimation and wall detection *IEEE J. Ocean. Eng.* **42** 532–43
[8] Martiny N, Sosnowski S, Kuhnlenz K, Hirche S, Nie Y, Jan-Moritz F and van Hemmen L 2009 Design of a lateral-line sensor for an autonomous underwater vehicle *IFAC Proc.* **42** 292–7
[9] Schwalbe A, Sevey J and Webb F 2016 Detection of artificial water flows by the lateral line system of a benthic feeding cichlid fish *J. Exp. Biol.* **219** 1050
[10] Xingan W and Aijun M 2007 The progress of studies on the relationship between feeding behavior and chemical or mechanical sense in fish *Prog. Fishery Sci.* **28** 104–8
[11] Liu G, Wang M, Wang A, Wang S, Yang T, Malekian R and Li Z 2018 Research on flow field perception based on artificial lateral line sensor system *Sensors* **18** 8
[12] Jiang Y, Ma Z, Fu J and Zhang D 2017 Development of a flexible artificial lateral line canal system for hydrodynamic pressure detection *Sensors* **17** 1220
[13] Fu J, Jiang Y and Zhang D 2016 PVDF based artificial canal lateral line for underwater detection *Sensors* **2015** 1–4
[14] Bleckmann H and Zelick R 2006 Lateral line system of fish *Integr. Zool* **4** 13
[15] Abdulsadda T, Zhang F and Tan X 2011 Localization of source with unknown amplitude using IPMC sensor arrays *Proc. SPIE* **7976** 797627
[16] Devries L, Lagor D, Lei H, Tan X and Paley A 2015 Distributed flow estimation and closed-loop control of an underwater vehicle with a multi-modal artificial lateral line *Bioinspir. Biomim.* **10** 025002
[17] Coombs S and Conley A 1997 Dipole source localization by mottled sculpin-approach strategies *J. Comp. Physiol.* A **180** 387–99
[18] Coombs S and Conley A 1997 Dipole source localization by the mottled sculpin. II. The role of lateral line excitation patterns *J. Comp. Physiol.* A **180** 401–15
[19] Conley A and Coombs S 1998 Dipole source localization by mottled sculpin. III. Orientation after site-specific, unilateral denervation of the lateral line system *J. Comp. Physiol.* A **183** 335–44
[20] Janssen J and Corcoran J 1993 Lateral line stimuli can override vision to determine sun fish strike trajectory *J. Exp. Biol.* **176** 299–305
[21] Enger P S, Kalmijn A and Sand O 1989 *Behavioral Investigations on the Functions of the Lateral Line and Inner Ear in Predation* (New York: Springer) pp 575–87
[22] Yang Y, Chen J, Engel J, Pandya S, Chen N, Tucker C, Coombs S, Douglas L J and Chang L 2006 Distant touch hydrodynamic imaging with an artificial lateral line *Proc. Natl Acad. Sci. USA* **103** 18891–5
[23] Chen J, Engel J, Chen N and Pandya S 2006 Artificial lateral line and hydrodynamic object tracking *IEEE Int. Conf. on Micro Electro Mechanical Systems* pp 694–7
[24] Yang Y, Chen N, Tucker C, Pandya S, Jones D and Liu C 2008 Biomimetic flow sensing using artificial lateral lines *ASME Int. Mechanical Engineering Congress & Exposition* pp 1331–8
[25] Yang Y, Nguyen N, Chen N, Lockwood M, Tucker C, Hu H, Bleckmann H, Liu C and Jones D L 2010 Artificial lateral line with biomimetic neuromasts to emulate fish sensing *Bioinspir. Biomim.* **5** 16001
[26] Mcconney E, Chen N, Lu D, Hu H, Coombs S, Liu C and Tsukruk V 2009 Biologically inspired design of hydrogel-capped hair sensors for enhancedunderwater flow detection *Soft Matter* **5** 292–5
[27] Asadnia M, Kottapalli G, Miao J, Warkiani E and Triantafyllou M S 2015 Artificial fish skin of self-powered micro-electromechanical systems hair cells for sensing

hydrodynamic flow phenomena *J. R. Soc. Interface.* **12** 20150322
[28] Franosch J M, Hagedorn H J, Goulet J, Engelmann J and van Hemmen J L 2009 Wake tracking and the detection of vortex rings by the canal lateral line of fish *Phys. Rev. Lett.* **103** 078102
[29] Sosnowski S, Franosch J M P, Zhang L, Nie Y, Kuhnlenz K, Hirche S and Van Hemmen L 2010 Simulation of the underwater vehicle 'Snookie': navigating like a fish *Proc. 1st Int. Conf. on Applied Bionics and Biomechanics (ICABB 2010)* pp 1–8
[30] Pandya S, Yang Y, Jones L, Engel J and Liu C 2006 Multisensor processing algorithms for underwater dipole localization and tracking using MEMS artificial lateral-line sensors *EURASIP J. Adv. Signal Process.* **2006** 1–8
[31] Landau L 1983 *Fluid Mechanics* (Oxford: Pergamon Press)
[32] Abdulsadda T and Tan X 2013 Nonlinear estimation-based dipole source localization for artificial lateral line system *Bioinspir. Biomim.* **8** 026005
[33] Franosch P, Sichert B, Suttner D and Hemmen V 2005 Estimating position and velocity of a submerged moving object by the cruleed frog Xenopus and by fish—a cybernetic approach *Biol. Cybern.* **93** 231
[34] Goulet J, Engelmann J, Chagnaud P, Franosch M, Suttner D and Van Hemmen L 2008 Object localization through the lateral line system of fish: theory and experiment *J. Comp. Physiol.* A. **194** 1–17
[35] Glowacz A 2019 Fault diagnosis of single-phase induction motor based on acoustic signals *Mech. Syst. Signal Process.* **117** 65–80
[36] Glowacz A 2018 Acoustic based fault diagnosis of three-phase induction motor *Appl. Acous.* **137** 82–89